

## Momentum spectra of atmospheric pions, muons, electrons and positrons at balloon altitudes

A Codino<sup>†</sup>, M T Brunetti<sup>†</sup>, C Federico<sup>†</sup>, C Grimani<sup>†</sup>, M Lanfranchi<sup>†</sup>,  
 M Menichelli<sup>†</sup>, M Miozza<sup>†</sup>, R L Golden<sup>‡††</sup>, S J Stochaj<sup>‡</sup>, S A Stephens<sup>§</sup>,  
 J W Mitchell<sup>||</sup>, J F Ormes<sup>||</sup>, R E Streitmatter<sup>||</sup>, M Hof<sup>¶</sup>, C Pfeifer<sup>¶</sup>,  
 W Menn<sup>¶</sup>, M Simon<sup>¶</sup>, G Basini<sup>+</sup>, M Ricci<sup>+</sup>, F M Brancaccio<sup>\*</sup>, P Papini<sup>\*</sup>,  
 S Piccardi<sup>\*</sup>, P Spillantini<sup>\*</sup>, M P De Pascale<sup>‡</sup>, A Morselli<sup>‡</sup> and P Picozza<sup>‡</sup>

<sup>†</sup> Dipartimento di Fisica dell'Università and Sezione INFN di Perugia, Perugia, Italy

<sup>‡</sup> Particle Astrophysics Laboratory, New Mexico State University, Las Cruces, USA

<sup>§</sup> Tata Institute of Fundamental Research, Bombay, India

<sup>||</sup> NASA/Goddard Space Flight Center, Greenbelt, MD, USA

<sup>¶</sup> Universität Siegen, Siegen, Germany

<sup>+</sup> Laboratori Nazionali INFN di Frascati, Frascati, Italy

<sup>\*</sup> Dipartimento di Fisica dell'Università and Sezione INFN di Firenze, Firenze, Italy

<sup>‡</sup> Dipartimento di Fisica dell'Università Tor Vergata and Sezione INFN di Roma II, Roma, Italy

Received 26 February 1997, in final form 12 July 1997

**Abstract.** Momentum spectra of pions, muons, electrons and secondary positrons have been measured at an atmospheric depth of  $5.8 \text{ g cm}^{-2}$  with the same instrument. Data was collected by the Matter Antimatter Space Spectrometer of the New Mexico State University in a balloon flight in September 1991 at the rigidity cut-off of  $4.5 \text{ GV } c^{-1}$  in Fort Sumner, New Mexico.

The first measurement of the positive muon spectrum in the range  $0.15 \text{ GeV } c^{-1}$  to  $2 \text{ GeV } c^{-1}$  is reported in this paper. The spectral index above  $3 \text{ GeV } c^{-1}$  of the negative muon momentum spectrum of this measurement is  $-2.39 \pm 0.05$  in agreement with analytical cascade calculations which assume a primary proton kinetic energy spectrum with a slope of  $-2.74 \pm 0.02$  in the corresponding kinetic energy range. In the momentum interval  $300\text{--}700 \text{ MeV } c^{-1}$ , both negative and positive muon fluxes turn out to be larger than calculated fluxes by a factor of about 1.4.

The measurement of the secondary electron and positron energy spectra allows a reliable subtraction of the atmospheric background from the primary electron and positron fluxes which are affected by large uncertainties in most of the experiments. The energy spectra of the secondary particles reported here have the same systematic errors implying a higher relative accuracy with respect to those measurements made in different flights.

### 1. Introduction

The fluxes of various secondary particles of the cosmic radiation as a function of the atmospheric depth [1–4] have been measured in a series of balloon flights, made during the last decade. These measurements have been accomplished as a collateral goal of positron and antiproton search in the primary cosmic radiation.

Galactic cosmic rays diffusing towards the Earth are deflected by the geomagnetic field. No primary cosmic rays reach the top of the atmosphere below a particular value of rigidity

††Deceased.

(cut-off rigidity). Thus, cosmic rays observed at balloon altitudes below the geomagnetic cut-off are mainly generated by interactions of primary cosmic rays in the atmosphere overlying the apparatus; a fraction of them consists also of re-entrant albedo particles [5].

In this paper, we report measurements of momentum spectra of secondary electrons and positrons; positive and negative muons and negative pions in the momentum range 0.15–4 GeV  $c^{-1}$  for electrons and positrons, 0.15–2 GeV  $c^{-1}$  for positive muons, 0.15–20 GeV  $c^{-1}$  for negative muons and 5–15 GeV  $c^{-1}$  for negative pions. Preliminary results have been presented elsewhere [6].

Similar measurements limited to the electron and muon components in different experiments have been recently reported [7–9].

Several research areas may benefit from these measurements. In particular, we would like to mention: (1) the study of the contamination of primary cosmic rays in the atmosphere; (2) the atmospheric neutrino problem; (3) cascade calculations in the atmosphere; (4) propagation of cosmic rays through the atmosphere.

(1) The flux determination of primary positron and other rare cosmic-ray species carried out by balloon-borne experiments requires the correct subtraction of atmospheric background. For example, some differences in the measurements of positron–electron ratio [10, 11] in the primary cosmic radiation may be accounted for by using appropriate atmospheric subtraction.

(2) Some measurements of atmospheric neutrino flux in underground experiments [12, 13] show that the ratio of muon neutrinos to electron neutrinos is significantly smaller than the calculated ratio generated by cosmic ray interactions in the atmosphere [14–16]. Neutrinos are produced in pion and muon decays; therefore pion and muon flux determination allows crosschecks on calculated atmospheric neutrino fluxes.

(3) Calibration of Monte Carlo programs and analytical calculations of hadronic cascades in the atmosphere are important in underground experiments.

There are many calculations describing the propagation of cosmic rays in the atmosphere [7]. It is important to verify the accuracy of these calculations with the secondary particle fluxes at different atmospheric depths determined by experiment.

(4) The influence of the geomagnetic field on the propagation of primary cosmic rays through the atmosphere has been extensively investigated. The effect of the geomagnetic field on atmospheric particle production has been evaluated and discussed in the literature (see for example [17–19]). The present measurements allow us to discriminate among various geomagnetic cut-off models.

## 2. Description of the instrument

The payload of this flight is an upgraded version of that used in the antiproton discovery in 1979 [20] and is shown in figure 1.

It consists of a superconducting magnet equipped with eight multiwire proportional chambers (MWPCs) and two modules of drift chambers for a total of 19 detector planes in the direction of the maximum bending of the magnet and 11 planes in the perpendicular direction. MWPCs use the delay-line readout technique. The magnet generates a maximum magnetic field of 2.2 T in the MWPC and drift chamber region. The spectrometer measures the particle deflection,  $\eta$ , and has an average maximum detectable rigidity (MDR) of 210 GV  $c^{-1}$ . A detailed description of the performance of MWPC and drift chamber systems is reported elsewhere [21, 22].

The tracking system is complemented with a time-of-flight (TOF) scintillator system, a gas Cherenkov detector and a streamer tube imaging calorimeter. The TOF counters consist

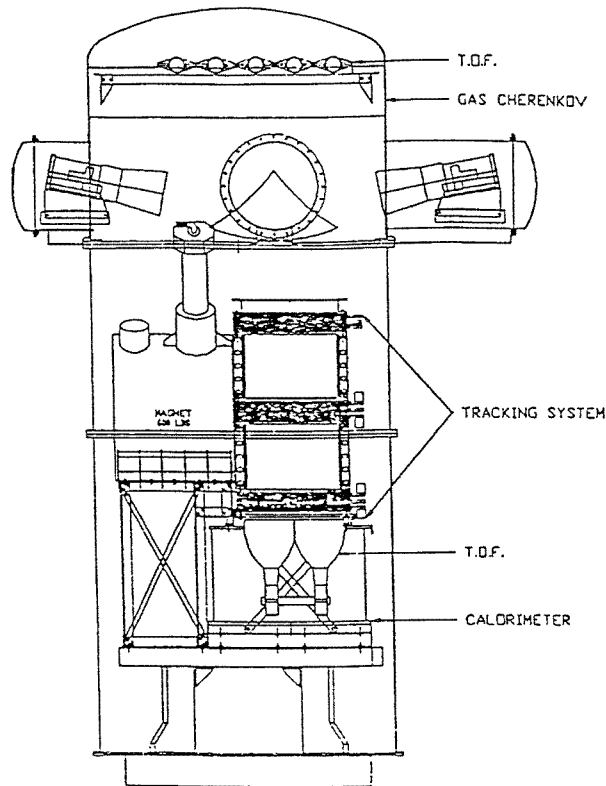


**Figure 1.** Cross section of the payload and detector arrangement used in this experiment. The instrument is enclosed in an aluminum cylinder of 0.5 cm average thickness, 3.8 m height and 1.5 m diameter. It consists of a TOF counter system, a Cherenkov detector, a magnetic spectrometer and a brass streamer-tube calorimeter.

of 12 plastic scintillator paddles (Bicron 404) arranged in three planes; two of them are located at the top of the instrument and the third is located below the chamber stack. The lever arm of the TOF system is 236 cm. This detector is used to determine the particle velocity and direction. The TOF resolution is 370 ps (rms) which assures an up-down rejection at more than 30 standard deviations.

The Cherenkov detector is located in a cylindrical box of 65 cm length filled with Freon 12 at a pressure of 760 Torr giving a threshold Lorentz factor of 23.5. This corresponds to  $2.5 \text{ GeV } c^{-1}$  for muons,  $3.3 \text{ GeV } c^{-1}$  for pions and  $22 \text{ GeV } c^{-1}$  for protons. The average number of photoelectrons produced by a particle well above the Cherenkov threshold is 18. The performance of the Cherenkov counter is described elsewhere [23].

The imaging calorimeter consists of 40 planes of 64 brass streamer tubes each, for a total of 7.3 radiation lengths and 0.75 nuclear interaction lengths. The calorimeter allows the reconstruction of the particle trajectories (for example see [24]) in two perpendicular sets of planes referred to as  $x$ -view (magnet bending direction) and  $y$ -view. The payload electric power is generated by lithium batteries and amounts to 1600 W. The entire payload weighs 2140 kg.

**Table 1.** Spectrometer selection criteria.

---

Criterion 1
At least 11 chambers in the direction of the maximum bending of the magnet ( <i>x</i> -view) and six chambers in the orthogonal plane ( <i>y</i> -view) give a good signal.
Criterion 2
The least-square fit of the reconstructed track must have $\chi_x^2 \leq 8$ and $\chi_y^2 \leq 8$ .
Criterion 3
The number of drift chamber planes with signals at more than 4 cm from particle trajectory has to be less than or equal to three in both views.
Criterion 4
The deflection error has to be less or equal to $0.03 (\text{GV } c^{-1})^{-1}$ .

---

### 3. Particle selection

In this section the selection criteria for the five particles  $\mu^-$ ,  $\mu^+$ ,  $e^-$ ,  $e^+$  and  $\pi^-$  are described.

The total number of triggers is 1057 729. Multiple track events in the chamber system, spurious signals and other detector effects reduce the original number of triggers to 378 974 events of electrons, muons, pions and other particles. The requirements reported in table 1 guarantee a good momentum measurement in the magnetic spectrometer.

#### 3.1. Electron and muon selection criteria below $1 \text{ GeV } c^{-1}$

Electron, positron and muon selection in the range  $0.15\text{--}1 \text{ GeV } c^{-1}$  requires the use of the TOF system and the Cherenkov counter. Electrons and muons are easily separated from protons and helium below  $1 \text{ GeV } c^{-1}$  (see figure 2). The TOF system allows the separation of muons and electrons from protons below  $2 \text{ GeV } c^{-1}$ . This results from the equation:

$$m^2 = R^2(1/\beta^2 - 1)$$

where  $m$ ,  $R$  and  $\beta$  are, respectively, the mass ( $\text{GeV } c^{-2}$ ), rigidity ( $\text{GV } c^{-1}$ ) and velocity of the particle traversing the apparatus. In figure 3 the square-mass distributions of muons, positrons and protons are shown.

The electron, positron and muon selection criteria are summarized in table 2.

#### 3.2. Electron, muon and pion selection criteria above $1 \text{ GeV } c^{-1}$

Electron, positron and muon candidates with momenta greater than  $1 \text{ GeV } c^{-1}$  as well as pions above  $5 \text{ GeV } c^{-1}$  are required to have a scintillator signal consistent with  $Z = 1$  particles in both top ( $Z_{\text{top}}$ ) and bottom scintillators ( $Z_{\text{bot}}$ ). A Cherenkov signal is also required for positrons, electrons and pions. Finally, the use of the calorimeter allows the separation of electromagnetic showers from hadronic cascades and non-interacting particles. Electrons interact in the calorimeter producing showers with high multiplicity secondaries showing small opening angles with respect to the incident-particle direction. The lateral spread of electron cascades is limited to two Molière radii, which in brass

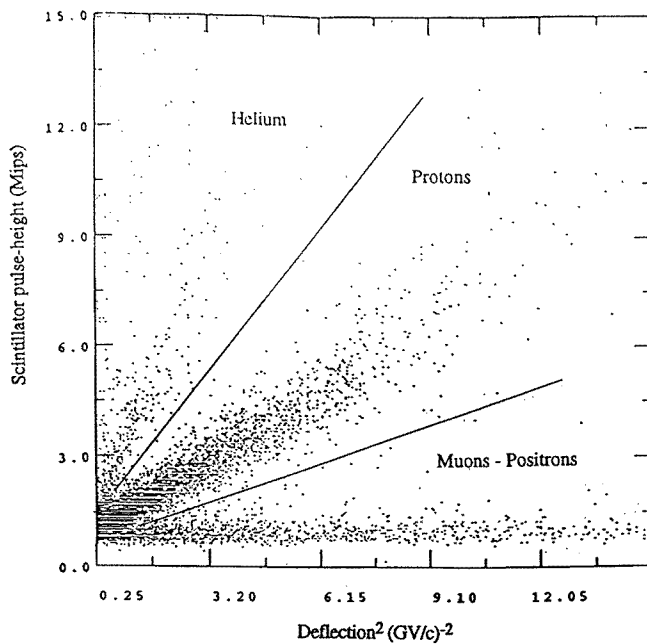


**Figure 2.** Scintillator pulse-height distribution versus deflection squared for helium, protons, muons and positrons for rigidities smaller than  $2 \text{ GV } c^{-1}$ .

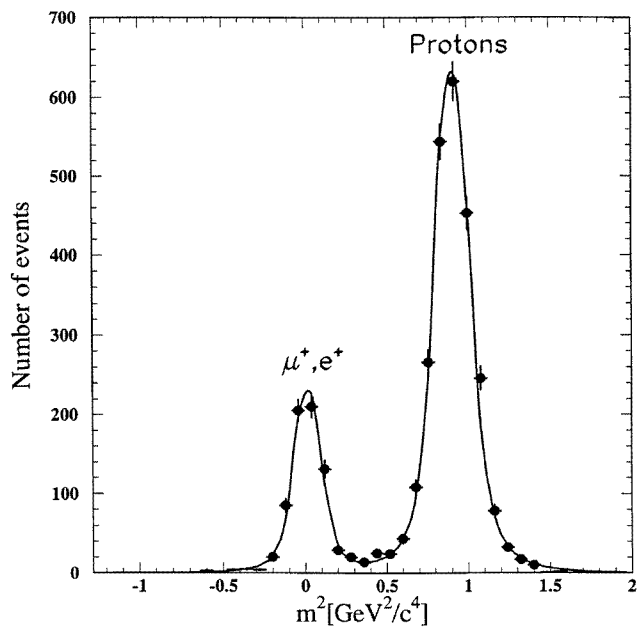


**Figure 3.** Square-mass distributions in the mass region of positive muons, positrons and protons determined by the TOF counter system. The full curve is the best line fit through the data.

is 3.2 cm. Hadronic cascades present lower multiplicity secondaries with larger opening angles. No secondaries are generated in the calorimeter by non-interacting particles, e.g.

**Table 2.** Electron, positron and muon selection criteria below 1 GeV  $c^{-1}$ .

---

Criterion 1
The scintillator signal is consistent with minimum ionizing particles with $Z = 1$ where $Z$ is the absolute electric charge.
Criterion 2
Electrons and positrons are separated from protons by requiring $m^2 \leq 0.3$ as shown in figure 3.
Criterion 3 for electrons and positrons
The Cherenkov signal is required to be above the Lorentz threshold of 23.5.
Criterion 4 for muons
No Cherenkov signal is required.

---

hadrons and muons.

Because of these different interaction topological characteristics, electromagnetic cascades are separated from hadronic showers and non-interacting particles on the basis of the number of calorimeter planes presenting two or more fired wires within two Molière radii from the shower axis extrapolated from the spectrometer. These multiple calorimeter hit wires per plane will be referred to as shower-clusters (see table 3). The optimum calorimeter cut for selecting non-interacting particles, has been obtained by studying a sample of 1000 non-interacting protons traversing the calorimeter. By comparing the calorimeter patterns generated by electron, muon-like, and interacting hadron samples we have found that interacting hadrons are separated from both electrons and muons according to criterion 5 of table 3.

Pion selection is restricted to interacting pions because negative muons are indistinguishable from non-interacting negative pions in the calorimeter.

Non-interacting protons are indistinguishable in the calorimeter from positive muons, therefore no positive muon analysis has been attempted above 2 GeV  $c^{-1}$ .

#### 4. Efficiencies and geometrical factor

Selection and detector efficiencies as well as the geometrical factor have to be taken into account in order to determine the absolute particle fluxes.

The spectrometer efficiency depends on particle rigidity. It ranges from  $72 \pm 2\%$  at 0.15 GV  $c^{-1}$  up to  $91 \pm 2\%$  above 5 GV  $c^{-1}$  for electrons and from  $71 \pm 2\%$  to  $93 \pm 2\%$  for muons in the same rigidity interval.

The cut efficiency of the particle-square mass is also rigidity dependent. It assumes the value 1 between 0.15 and 0.60 GV  $c^{-1}$  and then decreases to  $0.56 \pm 0.12$  at 2 GV  $c^{-1}$ .

The scintillator cut efficiency on the particle pulse height is 0.85 with an error smaller than 1% below 1 GV  $c^{-1}$ . Above 1 GV  $c^{-1}$ , the scintillator efficiency is  $0.91 \pm 0.01$  and that of the Cherenkov detector is 0.98.

The calorimeter selection efficiency is 1 for electrons and positrons in the momentum interval 1–2 GeV  $c^{-1}$  and 0.98 for those between 2 and 4 GeV  $c^{-1}$ . The calorimeter efficiency for muon selection is 0.95 with an error smaller than 1%. Inefficiency for muon detection of 5% in the calorimeter is due to delta rays and those streamer tubes fired by electronic noise. The calorimeter cut efficiency for interacting hadrons was determined by

**Table 3.** Selection criteria for electrons, positrons and muons above 1 GeV  $c^{-1}$  and for pions above 5 GeV  $c^{-1}$ .

---

 Criterion 1

 $Z_{\text{top}} \leq 1.8$  and  $Z_{\text{bot}} \leq 1.8$ .

Criterion 2 for electrons, positrons and pions

The Cherenkov signal is required to be above the Lorentz threshold of 23.5.

Criterion 3 for electrons and positrons

 (A) 1–2 GeV  $c^{-1}$ —A minimum of two calorimeter planes show shower-clusters in, at least, one calorimeter view.

 (B) 2–4 GeV  $c^{-1}$ —A minimum of four calorimeter planes show shower-clusters in, at least, one calorimeter view.

Criterion 4 for muons

No shower-cluster or at most one is present in each calorimeter view.

Criterion 5 for pions

(A) The maximum number of shower-clusters, in at least one calorimeter view, is greater than four and smaller than 12.

 (B) The shower opening angle in the calorimeter is greater than  $25^\circ$ .
 

---

applying the selection criteria listed in the previous paragraph to a sample of 500 interacting protons with momenta greater than 5 GeV  $c^{-1}$  and it was found to be  $0.60 \pm 0.04$ .

The requirement that, at least, one calorimeter view has a good quality track was taken into account for flux determination implying a calorimeter efficiency of 0.985.

The geometrical factor also varies with particle rigidity. In the rigidity interval 0.15–1 GV  $c^{-1}$ , the geometrical factor increases from 87 to 252 cm<sup>2</sup> sr and is constant and equal to 182 cm<sup>2</sup> sr for larger rigidities.

The acquisition trigger is activated by the scintillator-photomultiplier (PMs) system that has an overall efficiency of  $0.83 \pm 0.01$ . The total flight elapsed time for data analysis is 35 330 s. Data processing on board required 33% of the total exposure time of this flight of 9.8 hours. Therefore, the data acquisition efficiency is equal to 0.67.

## 5. Background estimates and results

### 5.1. Electron and positron background

The rate of accidental Cherenkov signal is 0.01 leading to a muon contamination of about 1% on the selected electron sample below 1 GV  $c^{-1}$ . In the same rigidity interval, the TOF system and Cherenkov selection criteria ensure a negligible contamination of hadrons.

The selected electron and positron samples of 522 and 303 events, respectively, above 1 GV  $c^{-1}$ , were scanned visually and non-interacting particles or low multiplicity secondary hadronic showers were not found. Therefore, an upper limit of 1% at 95% confidence level of background contamination can be estimated on the selected electron and positron samples.

### 5.2. Muon background

The contamination of negative muon events due to electrons amounts to 2% of the electron sample below 2 GeV (2717 events). The resulting subtraction is 5% at a few hundred MeV  $c^{-1}$  and 0.1% above 1 GeV  $c^{-1}$ . The contamination of positive muons due to protons surviving the square-mass cut (see section 3.1) is negligible at a few hundred MeV  $c^{-1}$ ; however, it increases to 39% at 2 GeV  $c^{-1}$ .

The expected atmospheric pion background [17] ranges from less than 1% below 1 GeV  $c^{-1}$  up to 10% above 10 GeV  $c^{-1}$ .

### 5.3. Pion background

The antiproton–negative pion ratio in cosmic rays at small atmospheric depth is 0.10 [1]. Antiprotons interacting in the calorimeter survive the pion identification criteria. Since antiprotons in the momentum range 5–15 GeV  $c^{-1}$  are below the Cherenkov threshold and the probability of spurious signals in the Cherenkov counter is 0.01, the antiproton contamination is unimportant.

The spectrometer resolution function for high-energy protons shows that the probability for protons to present negative curvature in the rigidity range 2–20 GV  $c^{-1}$  is less than  $10^{-3}$  [27].

## 6. Results

The resulting momentum spectra are shown in figure 4 for electrons and in figure 5 for positrons. Electron and positron energy spectra observed at small atmospheric depths in

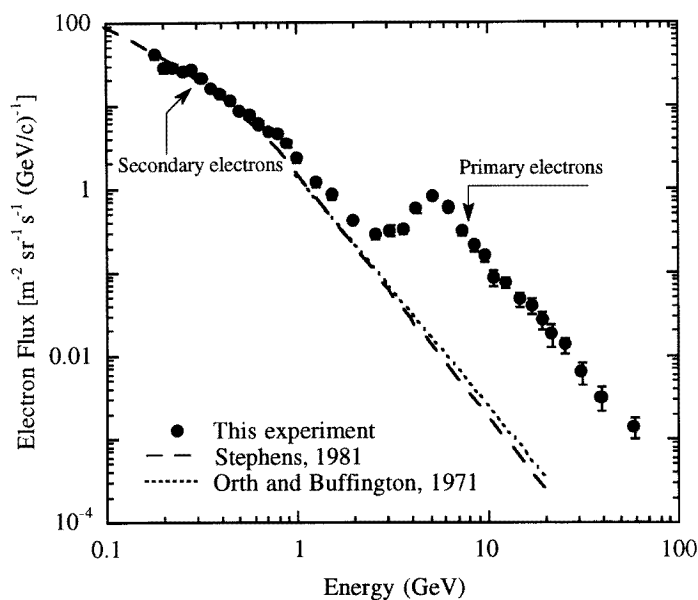


**Figure 4.** Electron energy spectrum measured by this experiment in the momentum range above 0.15 GeV  $c^{-1}$  at a depth of 5.8 g cm<sup>-2</sup> (full circles). Data are compared with theoretical calculations of the secondary electron flux estimated at the same depth (dotted and broken curves). Primary electrons dominate the atmospheric electron component above 4 GeV  $c^{-1}$ .

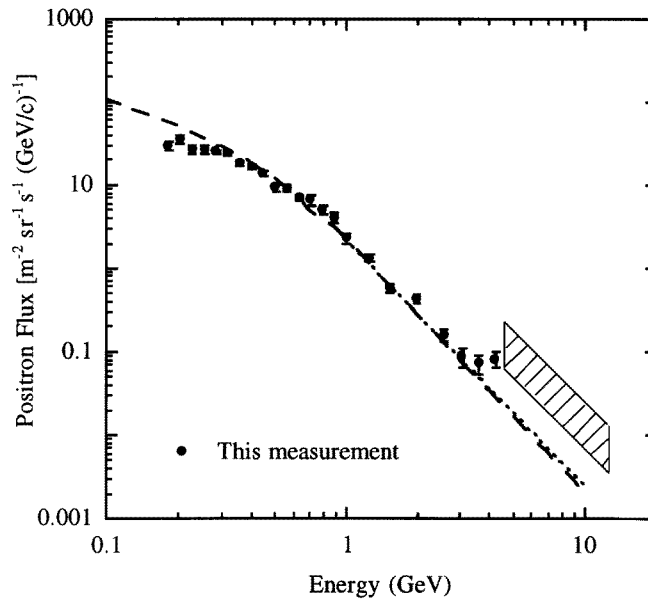


**Figure 5.** Secondary atmospheric positrons in the range  $0.15\text{--}4\text{ GeV } c^{-1}$  at a depth of  $5.8\text{ g cm}^{-2}$  (full circles). Data are compared with theoretical calculations (broken curve [17] and dotted curve [25]) at the same atmospheric depth. A contribution of ranged-down interstellar positrons can be noted above  $3\text{ GeV } c^{-1}$ . The dashed area represents the range of the expected primary positron flux according to previous measurements [11].

locations with high geomagnetic cut-off include, particles of secondary origin, produced in hadronic and electromagnetic showers in the atmosphere, primary electrons and positrons ranged down in energy and re-entrant albedo particles. While ranged down electrons, contributing to the secondary electron flux, is an important component, the observed positron flux mainly consists of pure secondary particles.

Note that the primary positron flux is approximately one tenth of the primary electron flux [11].

In figure 4, the primary electron spectrum measured by this experiment [26], has also been presented for comparison. Primary electrons dominate the spectrum above  $4\text{ GeV } c^{-1}$ . Note that the difference between the total electron flux and that of the secondary atmospheric electrons in the energy range  $2\text{--}5\text{ GeV}$ , close to the nominal cut-off of  $4.5\text{ GeV } c^{-1}$  (see the broken curve in figure 4) is due to primary electrons that have suffered energy losses (mainly bremsstrahlung) in the overlying atmosphere [28]. This circumstance implies that the re-entrant albedo electron flux is negligible [5].

The positive muon flux is shown in figure 6 and that of the negative muons in figure 7.

The negative muon spectrum shows a slope of  $-2.39 \pm 0.05$  above  $2\text{ GeV } c^{-1}$  and then it flattens at lower momentum values. In the same figure, the negative muon energy spectrum measured by the MASS experiment in 1989 has been also displayed [1]. That observation was carried out at  $5\text{ g cm}^{-2}$  of atmospheric depth, in Prince Albert (Canada) where the geomagnetic cut-off is  $650\text{ MV } c^{-1}$ . The two measurements above  $1\text{ GeV } c^{-1}$  show the same spectral index in agreement with predictions [17].

The reported calculations underestimate experimental data on the muon energy spectra determined at high geomagnetic cut-off by a factor of 1.4 in the momentum band  $300\text{--}$

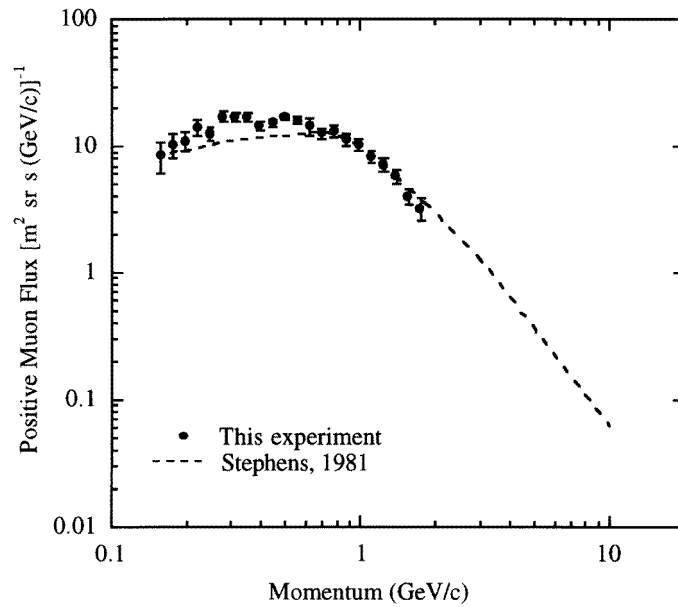


**Figure 6.** Positive muon flux measurement between 0.15 and 2  $\text{GeV c}^{-1}$  at  $5.8 \text{ g cm}^{-2}$  (full circles). The data are compared with theoretical calculations at the same atmospheric depth (broken curve).

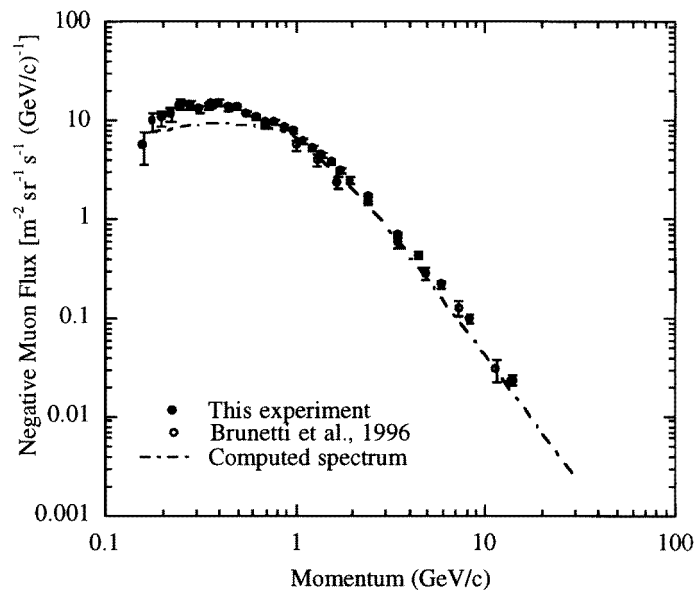


**Figure 7.** Negative muon flux measurement between 0.15 and 20  $\text{GeV c}^{-1}$  at  $5.8 \text{ g cm}^{-2}$ . Data (full circles) are compared with calculations (chain curve) made at the same atmospheric depth [17]. The results of a previous measurement (MASS apparatus) at  $5 \text{ g cm}^{-2}$  of overlying atmosphere and a rigidity cut-off of  $0.650 \text{ GV c}^{-1}$  have been also reported (open circles).

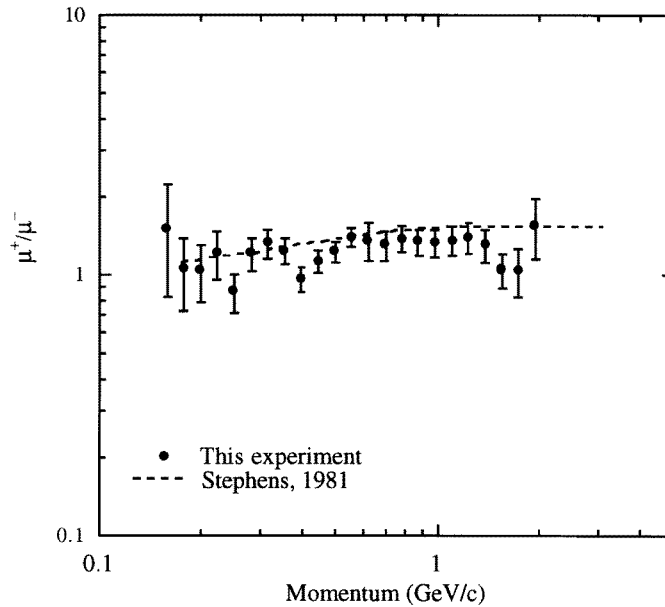


**Figure 8.** Positive–negative muon ratio at  $5.8 \text{ g cm}^{-2}$  of atmospheric depth (full circles). Data are compared with theoretical calculations carried out at the same atmospheric depth (broken curve).

$700 \text{ MeV } c^{-1}$ . The calculations of muon spectra utilize a simplified model for the geomagnetic cut-off (step function) and an oversimplification of the invariant cross section of charged pion production in pp collisions. These approximations might explain the differences between the computed and measured muon spectra.

The positive–negative muon ratio has also been determined and is displayed in figure 8. This observation, above  $700 \text{ MeV } c^{-1}$ , seems to be lower than the reported calculated ratio. However, measurements with smaller statistical errors are needed in order to assess if calculations overestimate the positive muon component at small atmospheric depths.

The absolute negative pion flux is determined by correcting the observed number of events with the  $\pi^-$  interaction probability in the calorimeter. This probability is calculated by using the inelastic cross section of pions on deuterium scaled to a target having the same atomic number of the calorimeter. The resulting interaction probability in the calorimeter is 0.39. The pion differential flux based on nine observed events is given in figure 9. It presents large error bars due to the small number of pions observed in this flight. The measured flux is not in disagreement with calculations [17] and reinforces the previous measurement made in 1989 [1].

To our knowledge the calculations shown in figures 4–9 are the only published calculations at very small atmospheric depths for all the secondaries studied in this paper. The primary cosmic-ray energy spectrum utilized in the calculation mentioned above has been taken from data published at a minimum of solar modulation prior to 1981. Recent measurements made by the LEAP [28] and BESS [29] collaborations indicate that primary proton and helium fluxes are about 20% lower than previous measurements [30]. This decrease in the fluxes has not been confirmed by a recent measurement of the IMAX experiment [31], which, in contrast, agrees with older measurements. For these motivations the use of calculations by Stephens is believed plausible. Note that primary heavy nuclei

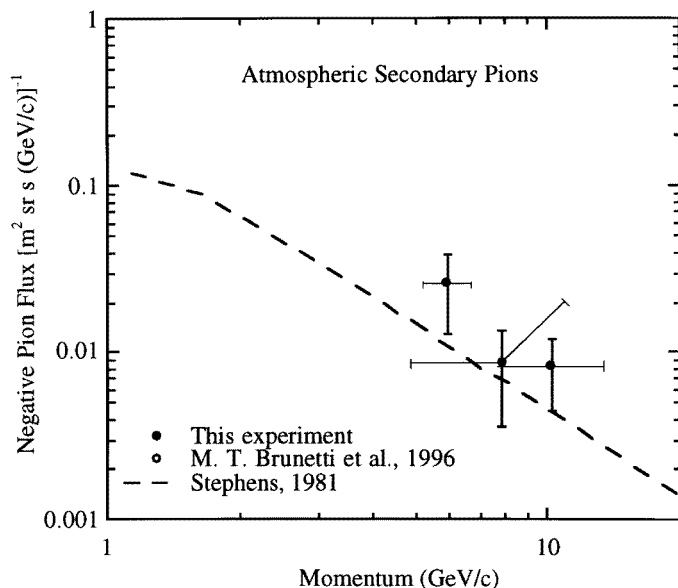


**Figure 9.** Measured negative pion differential flux at  $5.8 \text{ g cm}^{-2}$  of atmospheric depth (full circles). Data are compared with a previous measurement made by the MASS experiment at  $5 \text{ g cm}^{-2}$  (open circles) and to theoretical calculations extrapolated at  $5.8 \text{ g cm}^{-2}$  of atmospheric depth (broken curve).

have been taken into account in the quoted calculations.

The best avenue to crosscheck calculations is to measure the secondary particle fluxes at small atmospheric depths. Incorrect calculations of the secondary atmospheric components may entail incorrect measurements of rare primary particles such as positrons and antiprotons made by balloon-borne instruments. For example, a maximum difference of a factor of 4 between different calculations of secondary atmospheric electron and positron fluxes in the energy interval 1–30 GeV have been reported [7]. These differences give rise to an uncertainty on the  $e^+/(e^+ + e^-)$  primary ratio of up to a factor of 2 in the same energy interval.

According to the quoted calculations, at an atmospheric depth of  $5 \text{ g cm}^{-2}$  and a few GeV of energy, secondary electrons are only about 1% of the whole electron flux, while more than 10% of the total positron flux consists of secondary positrons (see [11, table 3]). If the calculated fractions of secondary atmospheric electrons and secondary atmospheric positrons are increased by a factor of four (e.g. 4% for electrons and 40% for positrons) the resulting  $e^+/(e^+ + e^-)$  primary ratio would decrease by 25% .

The secondary atmospheric antiproton flux has a notable influence on the primary antiproton–proton ratio. At an atmospheric depth of  $5 \text{ g cm}^{-2}$  and an energy of about 10 GeV the secondary atmospheric antiproton flux is 25% of the total antiproton flux [32]. Though the atmospheric secondary antiproton flux has not yet been determined in this flight (nor has it been in any other experiment), the secondary particle fluxes observed in this measurement also constrain the calculated secondary antiproton flux.

Additional flux measurements of secondary atmospheric particles at different geomagnetic cut-offs and various solar modulation conditions would complement the results of this experiment. In particular, a measurement of the secondary antiproton flux generated in the atmosphere well below the geomagnetic cut-off is desirable. Its subtraction from that

of primary antiprotons would significantly reduce the large error bars present in all available antiproton measurements.

## References

- [1] Brunetti M T *et al* 1996 *J. Phys. G: Nucl. Part. Phys.* **22** 145
- [2] Bellotti R *et al* 1996 *Phys. Rev. D* **53** 35
- [3] Golden R L *et al* 1995 *J. Geophys. Res.* **100** 515
- [4] De Pascale M P *et al* 1993 *J. Geophys. Res.* **98** 3501
- [5] Dev Verma S 1967 *J. Geophys. Res.* **72** 915
- [6] Grimani C *et al* 1995 *Conf. Paper 24th Int. Cosmic Ray Conf.* **4** 1029
- [7] De Nolfo G *et al* 1995 *Paper 24th Int. Cosmic Ray Conf.* **1** 589
- [8] Krizmanic J F *et al* 1995 *Conf. Paper 24th Int. Cosmic Ray Conf.* **1** 593
- [9] Schneider E *et al* 1995 *Conf. Paper 24th Int. Cosmic Ray Conf.* **1** 690
- [10] Barwick S W *et al* 1995 *Phys. Rev. D* **75** 390
- [11] Golden R L *et al* 1994 *Astrophys. J.* **436** 769
- [12] Becker-Szendy R *et al* 1992 *Phys. Rev. D* **46** 3720
- [13] Fukada Y *et al* 1994 *Phys. Lett. B* **335** 237
- [14] Barr G, Gaisser T and Stanev T 1989 *Phys. Rev. D* **39** 3532
- [15] Lee H and Koh Y S 1990 *Nuovo Cimento B* **105** 883
- [16] Honda M. 1990 *Phys. Lett. B* **248** 193
- [17] Stephens A S 1981 *Conf. Paper 17th Int. Cosmic Ray Conf.* **4** 282
- [18] Papini P, Grimani C and Stephens A S 1995 *Conf. Paper 24th Int. Cosmic Ray Conf.* **4** 1047
- [19] Gaisser T K and Stanev T 1995 *Conf. Paper 24th Int. Cosmic Ray Conf.* **1** 694
- [20] Golden R L *et al* 1979 *Phys. Rev. Lett.* **43** 1196
- [21] Golden R L *et al* 1991 *Nucl. Instrum. Methods Phys. Res. A* **306** 366
- [22] Hof M *et al* 1994 *Nucl. Instrum. Methods Phys. Res. A* **345** 561
- [23] Golden R L *et al* 1995 *PAL Technical Note #224* available on request
- [24] Codino A *et al* 1988 *Nuovo Cimento B* **103** 319
- [25] Orth C D and Buffington A 1971 *Astrophys. J.* **164** 529
- [26] Codino A *et al* 1997 *Conf. Paper Vulcano Workshop 1996 (Nuovo Cimento)* p 447
- [27] Papini P 1996 *PhD Thesis* University of Florence, Italy
- [28] Codino A *et al* 1997 Absolute positron and electron spectra in the primary cosmic radiation above 7 GeV to be submitted to *Astrophys. J. Lett.*
- [29] Seo E S *et al* 1995 *Conf. Paper 24th Int. Cosmic Ray Conf.* **2** 648
- [30] Papini P *et al* 1996 *Nuovo Cimento* **19C** 367
- [31] Menn W *et al* 1997 *Conf. Paper 25th Int. Cosmic Ray Conf.* **4** 390
- [32] Hof M *et al* 1996 *Astrophys. J.* **467** L33–6